THE DUST-SCATTERED X-RAY HALO AROUND *SWIFT* GRB 050724

S. Vaughan,[1] R. Willingale,[1] P. Romano,[2] J. P. Osborne,[1] M. R. Goad,[1] A. P. Beardmore,[1]
D. N. Burrows,[3] S. Campana,[2] G. Chincarini,[2,4] S. Covino,[2] A. Moretti,[2] P. T. O'Brien,[1]
K. L. Page,[1] M. A. Supper,[1] and G. Tagliaferri[2]

ABSTRACT

This paper discusses the X-ray halo around the *Swift* γ-ray burst GRB 050724 ($z = 0.258$), detected by the *Swift* X-Ray Telescope. The halo, which forms a ring around the fading X-ray source, expands to a radius of $200''$ within 8 ks of the burst, exactly as expected for small-angle X-ray scattering by Galactic dust along the line of sight to a cosmologically distant GRB. The expansion curve and radial profile of the halo constrain the scattering dust to be concentrated at a distance of $D = 139 \pm 9$ pc (from Earth) in a cloud/sheet of thickness $\Delta D < 22$ pc. The halo was observed only out to scattering angles of $200''$, for which the scattering is dominated by the largest grains, with a maximum size estimated to be $a_{\max} \approx 0.4$–0.5 μm. The scattering-to-extinction ratio was estimated to be $\tau_{\mathrm{scat}}/A_V \gtrsim 0.022$; this is a lower limit to the true value because contribution from smaller grains, which scatter to larger angles, was not directly observed. The line of sight to the GRB passes close to the Ophiuchus molecular cloud complex, which provides a plausible site for the scattering dust.

Subject headings: dust, extinction — Galaxy: structure — gamma rays: bursts — X-rays: general

Online material: color figures

1. INTRODUCTION

Small-angle scattering of X-rays by dust grains can produce a "halo" around a distant X-ray source, with a radial intensity distribution that depends on the dust properties and location (Overbeck 1965; Hayakawa 1970; Trümper & Schönfelder 1973). This effect was first detected by Rolf (1983) using *Einstein* observations of the bright X-ray binary GX 339$-$4 and has subsequently been observed around several other bright Galactic X-ray sources (e.g., Catura 1983; Predehl & Schmitt 1995; Predehl et al. 2000).

Gamma-ray bursts (GRBs) produce high X-ray fluxes for short periods, typically $\lesssim 1000$ s. Viewed through a substantial column of Galactic dust, these impulsive X-ray events may produce halos that appear to expand on the sky because X-rays scattered at larger angles travel a slightly longer path length to the observer and suffer an increased time delay. This time delay, between the direct and scattered light, means that the later observations of the scattered light provide a view of the GRB X-ray emission at earlier times and can, in principle, provide details of the location, spatial distribution, and properties of the dust (e.g., Alcock & Hatchett 1978; Klose 1994; Miralda-Escudé 1999; Draine & Bond 2004). In particular, assuming the GRB to lie at a cosmological distance, the distance to the scattering dust can be measured from the radial expansion of the halo, because the halo size increases as $\theta^2 = 2\tau c/D$, where $\tau = t - t_X$ is the time since the pulse of illuminating X-rays, and D is the distance between the dust and observer. Observations of GRB dust halos can thereby provide very accurate distances to Galactic structures, as first demonstrated by Vaughan et al. (2004) using an *XMM-Newton* observation of the

International Gamma-Ray Astrophysics Laboratory (*INTEGRAL*) GRB 031203.

This paper discusses the X-ray halo around GRB 050724, the first halo discovered by *Swift* (Romano et al. 2005) and only the second ever observed around a GRB. The rest of the paper is organized as follows: § 2 discusses the *Swift* observations and basic data analysis; § 3 describes the X-ray properties of the burst counterpart during the first few kiloseconds of the observation; § 4 discusses the detailed analysis of the X-ray halo images; § 5 uses the archival *Röntgensatellit* (*ROSAT*) and *Infrared Astronomical Satellite* (*IRAS*) data to probe the interstellar medium (ISM) in the direction of the GRB; and finally, the implications of the results of this analysis are discussed in § 6. Throughout this paper the quoted errors correspond to 90% confidence regions, unless stated otherwise.

2. OBSERVATIONS AND DATA ANALYSIS

At 2005 July 24 12:34:09 UT, the *Swift* (Gehrels et al. 2004) Burst Alert Telescope (BAT; Barthelmy 2004) triggered and located GRB 050724 (Covino et al. 2005). The prompt BAT light curve showed a relatively short-lived spike, with a FWHM of ≈ 0.25 s (Covino et al. 2005; Krimm et al. 2005), plus an extended low-flux tail lasting for at least $\gtrsim 200$ s. As discussed by Barthelmy et al. (2005), this burst would have been classified a short burst if observed by the Burst and Transient Source Experiment (BATSE). The total fluence was $\approx (6.3 \pm 1.0) \times 10^{-7}$ ergs cm^{-2} (Krimm et al. 2005) over the 15–350 keV band. The spectrum evolves from relatively hard during the 1 s peak (photon index of $\Gamma = 1.71 \pm 0.16$) to much softer ($\Gamma = 2.5 \pm 0.2$) at 50–150 s after the trigger.

The spacecraft slewed immediately to the BAT onboard calculated position; the *Swift* X-Ray Telescope (XRT; Burrows et al. 2004, 2005a) began observations at 12:35:22.9 UT (in automatic state), only 74 s after the BAT trigger, and detected a rapidly fading, uncataloged X-ray source at (J2000) R.A. = $16^{\mathrm{h}}24^{\mathrm{m}}44\overset{\mathrm{s}}{.}4$, decl. = $-27°32'28''$ (with a 90% confidence radius of $6''$; Barthelmy et al. 2005). This position is close to the Galactic

[1] X-Ray and Observational Astronomy Group, University of Leicester, Leicester LE1 7RH, UK; sav2@star.le.ac.uk.
[2] INAF—Osservatorio Astronomico di Brera, Via Bianchi 46, 23807 Merate, Italy.
[3] Department of Astronomy and Astrophysics, Pennsylvania State University, 525 Davey Lab, University Park, PA 16802.
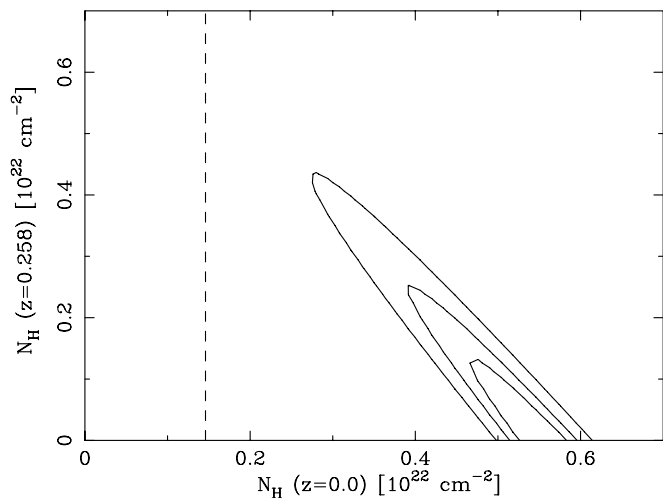[4] Universitá degli studi di Milano-Bicocca, Dipartimento di Fisica, Piazza delle Scienze 3, I-20126 Milan, Italy.

Fig. 1.—The $\Delta\chi^2$ contours for absorption in the host Galaxy ($z = 0.258$) against Galactic absorption ($z = 0.0$). The contours correspond to $\Delta\chi^2 = 2.30$, 4.61, and 9.21, respectively. The dashed line indicates the expected N_H based on the 21 cm measurements of Dickey & Lockman (1990).

plane ($l = 350°.37$, $b = +15°.10$); the expected column density of neutral Galactic gas along this line of sight (LOS) is $N_H = 1.46 \times 10^{21}$ cm^{-2} (as measured from 21 cm maps; Dickey & Lockman 1990), and the reddening $E(B - V) = 0.59$ (from the IR dust maps of Schlegel et al. 1998).

Follow-up observations revealed a variable optical and radio source within the XRT error circle (4″.3 from the XRT position; Gal-Yam et al. 2005; Soderberg et al. 2005). A 50 ks *Chandra* observation further refined the position of the fading X-ray source and showed it to be coincident with the optical and radio transient (Burrows et al. 2005b). Prochaska et al. (2005) identified the host galaxy of the transient to be a massive early-type galaxy at a redshift of $z = 0.258 \pm 0.002$ (from Ca H+K and G-band absorption; see also Berger et al. [2005] for a discussion of the host galaxy optical spectrum).

The XRT collected data in windowed-timing (WT) mode from 79–342 s postburst, after which time the data were taken in photon-counting (PC) mode. WT mode allows imaging in one spatial dimension only, whereas PC mode produces two-dimensional images; see Hill et al. (2004) for a full description of the XRT operating modes. The XRT data were processed by the *Swift* Data Center at NASA/Goddard Space Flight Center (GSFC) to level 1 data products (calibrated, quality flagged event lists). These were

further processed with `xrtpipeline` version 0.8.8 into level 2 data products. In the subsequent analysis, only event grades 0–2 were used for the WT mode data, and only grades 0–12 were used for the PC mode data.

3. EARLY X-RAY EMISSION FROM GRB 050724

Spectra and light curves were extracted from the WT data using a 40 pixel (94″) wide box to define the source and background regions. For the PC mode data, source counts were accumulated from within a circle of radius 25 pixels (59″), and background data were accumulated within an annulus having inner and outer radii of 60 and 100 pixels (141″–236″). The appropriate ancillary response matrices were generated using `xrtmkarf` version 0.4.14.

The spectrum of the WT data (79–342 s postburst) was binned such that each spectral bin contained at least 20 counts and fitted over the 0.6–10 keV range using XSPEC (Arnaud 1996).[5] The spectral model comprised a power-law continuum modified by two neutral absorbers (modeled using the TBabs code of Wilms et al. 2000), one at $z = 0.0$ and the other at $z = 0.258$, corresponding to neutral interstellar gas in our Galaxy and intrinsic to the GRB host galaxy, respectively. Allowing both column densities to be free parameters, this simple model gave a very good fit ($\chi^2 = 355.89$ for 334 degrees of freedom [dof]), with best-fitting parameters as follows: $\Gamma = 1.94 \pm 0.05$, $N_H(z = 0.0) = 5.9^{+0.3}_{-1.5} \times 10^{21}$ cm^{-2}, and $N_H(z = 0.258) < 2.4 \times 10^{21}$ cm^{-2}. The Galactic column density inferred from the X-ray spectrum exceeds that expected based on the 21 cm measurements (see § 2) by $4.4^{+0.3}_{-1.5} \times 10^{21}$ cm^{-2}, and yet there is no clear excess absorption intrinsic to the host galaxy. Figure 1 shows the $\Delta\chi^2$ contours for the two absorption column densities.

4. X-RAY HALO ANALYSIS

4.1. *Expansion Curve*

Figure 2 shows the XRT (PC mode) images from the first, second, and later orbits of *Swift*, over the 0.2–5 keV energy range (only events with energies 0.2–5 keV were used, since the halo has a soft spectrum, as discussed in § 4.3, and was not detected above 5 keV). The first orbit showed extended emission around the pointlike GRB, which was dispersed in the second orbit and

---

[5] The bandpass for the WT mode spectral fit was restricted to energies above 0.6 keV to avoid calibration uncertainties at lower energies.
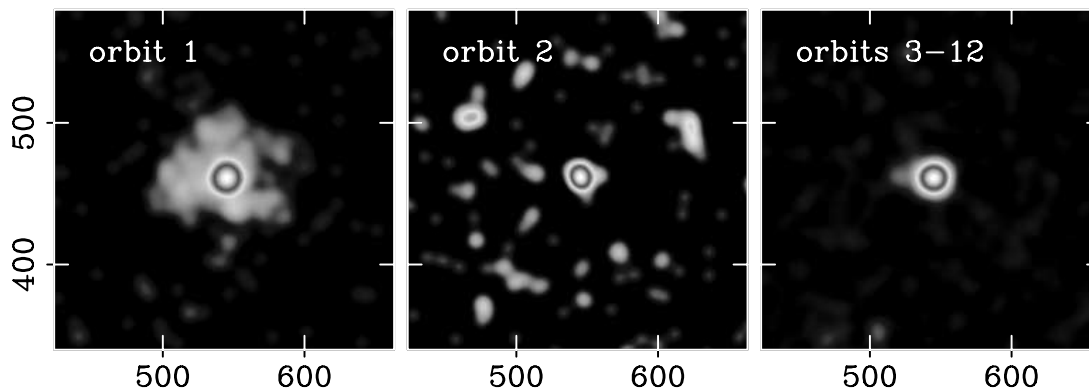

Fig. 2.—XRT images (0.2–5 keV) of GRB 050724 taken in three time intervals, covering the first orbit (343–2243 s after T_0), second orbit (6068–8127 s after T_0), and later orbits of *Swift*, plotted in detector coordinates. The images were smoothed using a Gaussian of width 5 pixels (σ). The X-ray counterpart of GRB 050724 is in the center of each frame. During orbit 1 the halo expands from a radius of 20 to 44 pixels, during orbit 2 it is visible as a faint ring with a radius of ∼85 pixels, and in later orbits the halo is not detected. [*See the electronic edition of the Journal for a color version of this figure.*]
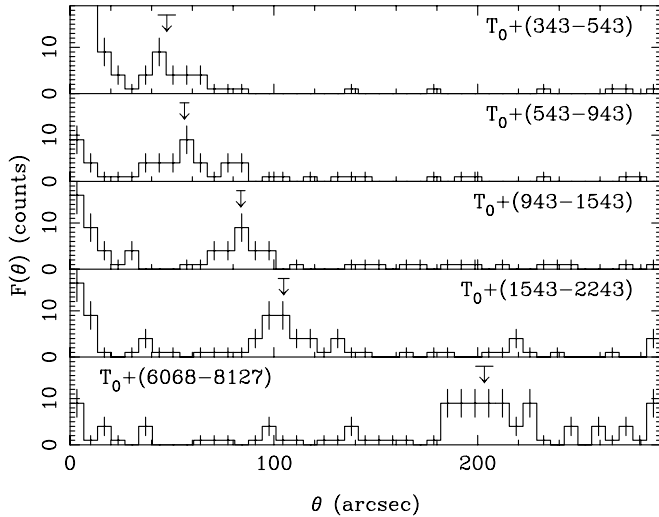
FIG. 3.—Radial profile of counts about the GRB 050724 afterglow from five time intervals. The times are marked in each frame. The arrows mark the maximum likelihood estimate of the halo radius, θ, derived from fitting these profiles, and the horizontal bar indicates the 68.3% (1 σ) confidence interval on the radius.
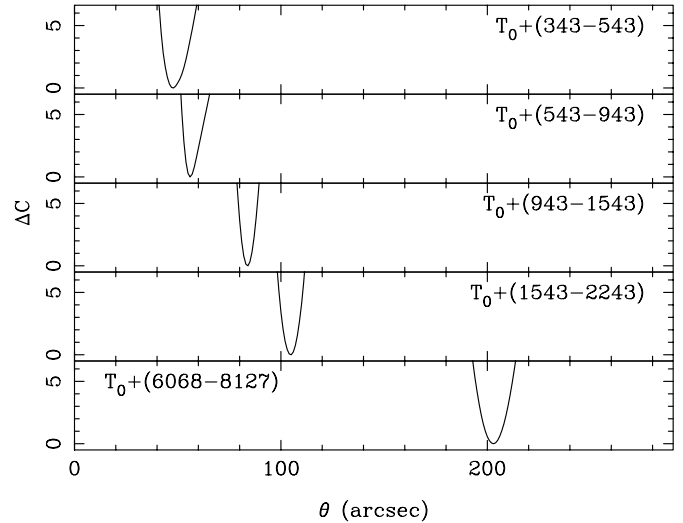

FIG. 4.—Change in C-statistic as a function of halo position. The minimum of each curve represents the maximum likelihood estimate of the halo radius. Nominal 68.3% and 90% confidence regions can be defined by the intervals bounded by $\Delta C = 1.0$ and 2.706, respectively.

was difficult to detect in later orbits. In order to better quantify this extension, images were accumulated in five nonoverlapping time intervals: 343–543, 543–943, 943–1543, and 1543–2243 s from the first orbit; and 6068–8127 s from the second orbit.

Radial profiles were calculated for each image by accumulating the counts in annuli centered on the GRB (see Fig. 3). The expanding halo was revealed by the small but significant localized excess of counts, beyond the unresolved GRB.[6] The radius of the halo as a function of time, $\theta(t)$, was estimated by fitting each radial profile (using XSPEC) with a model comprising the PSF of the source (a King profile with parameters taken from ground-based calibration data; Moretti et al. 2004, 2006) plus a constant background level (per pixel), integrated over the annular bin. A Gaussian was added to represent the profile of the halo, fixing the width to be equal to 10% of the radius: $\sigma_\theta = 0.1\theta$ (see § 4.2). The C-statistic was used to find the maximum likelihood model parameters, appropriate for the case of a few counts per bin ($C = -2 \log \mathcal{L}$, where $\mathcal{L}$ is the likelihood; Cash 1979). For each profile, the C-statistic was minimized, and the maximum likelihood position of the Gaussian was used as the radius of the halo in that image. The 90% confidence region for the radius was estimated using the ΔC values (see Fig. 4).

Figure 5 shows the radius of the halo in each of the five time bins, as measured using the radial profiles. These data were fitted with the function $\theta(t) = N(t - t_X)^{1/2}$, which describes the radial expansion of a dust-scattered halo following a (short) X-ray pulse at time t_X (e.g., Trümper & Schönfelder 1973; Klose 1994; Miralda-Escudé 1999; Draine & Bond 2004). Strictly speaking, this assumes a very narrow pulse of X-rays and an intrinsically narrow dust-scattering screen. The value of t_X corresponds to the typical arrival time of direct (unscattered) photons, which will be after T_0, since GRB 050724 remained X-ray bright from T_0 until $\approx T_0 + 300$ s, meaning almost all the direct X-rays actually arrived after T_0. The best-fitting values of the free parameters were $N = 2.46 \pm 0.08$ (with θ measured in arcseconds) and $t_X = 145^{+65}_{-74}$ s after T_0. This model gave a good fit, with $\chi^2 = 6.70$ for 4 dof. In order

to check whether the best-fitting value of t_X is plausible, the mean arrival time for the direct X-rays was estimated using the X-ray light curve from the joint BAT/XRT data (Fig. 3 of Barthelmy et al. 2005): the flux-weighted photon arrival time[7] over this light curve was $T_0 + 86$ s, consistent with the best-fitting t_X from the radial expansion curve.

The normalization N describes how fast the halo expands and is uniquely determined by the distance to the dust.[8] Assuming the GRB to be at a cosmological distance, $N = (2c/D)^{1/2}$. The best-fitting normalization predicts a distance to the scattering medium

---

[6] The point-spread function (PSF) of the XRT has a half-energy radius of $\approx 8\farcs8$, or FWHM $\approx 9\farcs6$, at $E \approx 1.5$ keV (Moretti et al. 2006; Burrows et al. 2004).

[7] The flux-weighted photon arrival time was calculated as $\langle t_X \rangle = \int f_X(t) t \, dt / \int f_X(t) \, dt$, where $f_X(t)$ is the X-ray light curve.
[8] The halo shape is affected by the geometry of the scattering region, and it may not be circular and centered on the GRB image if the scatterer is in the form of a plane-parallel slab not perpendicular to the LOS or is curved (see Tylenda 2004 for a discussion). However, because of the large ratio of dust distance to halo size, only the most pathological geometries (e.g., slab inclined at $>89°$) will produce any observable effect.
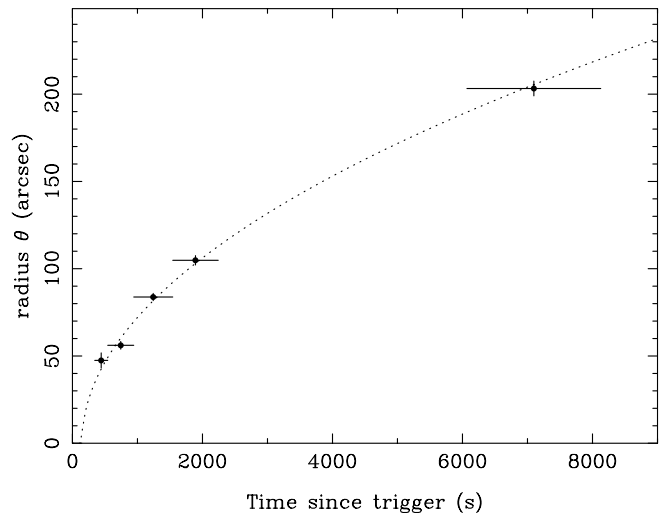

FIG. 5.—Expansion of the ring around GRB 050724 with time. The radii were measured by fitting the local maximum in the radial profiles (Fig. 3). The expansion was fitted with the function $\theta(t) = N(t - t_X)^{1/2}$ (dotted line).
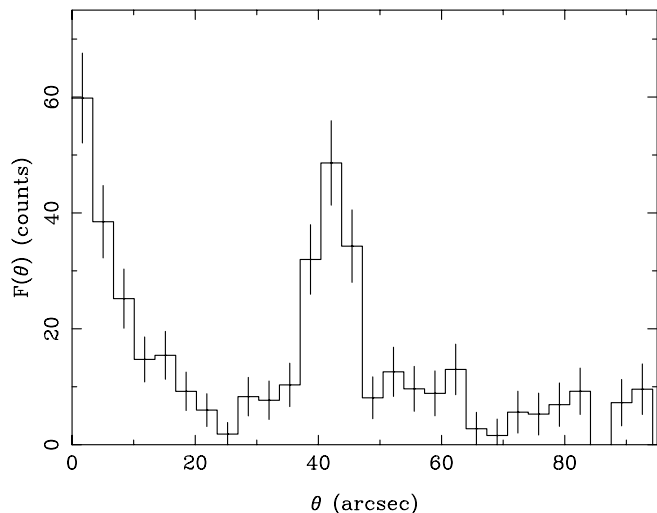
Fig. 6.—Comoving radial profile around GRB 050724. This shows the counts accumulated in annuli around the GRB summed over the five time intervals of Fig. 3, after correcting for the expansion of the halo (matching the radii to those from the first image). The halo occurs at $\theta \approx 45''$ from the GRB ($\theta = 0$).
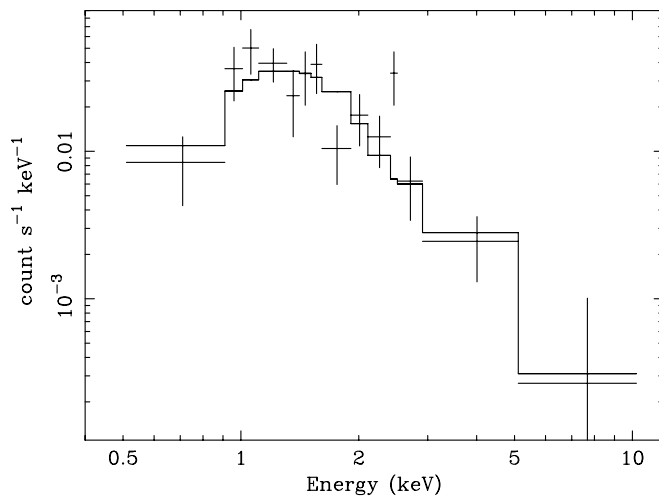

Fig. 7.—XRT spectrum of the halo during the first *Swift* orbit. Crosses mark the data, and the histogram marks the best-fitting absorbed power-law model. The data were binned for illustration purposes only.

of $D = 139 \pm 9$ pc, where the 90% confidence region was calculated with t_X as a free parameter.[9]

This distance measurement is quite robust to the choice of function used to parameterize the halo radial profile. This was demonstrated by repeating the radial profile fitting using different functions to model the halo profile. For each one, the halo expansion curve was measured and the distance was calculated from its best-fitting normalization. A Gaussian of fixed width ($\sigma = 5''$) gave $D = 145 \pm 8$ pc, a Lorentzian of fixed width ($\Gamma = 10''$) gave $D = 142 \pm 8$ pc, and a King model as used to model the PSF (see above) gave $D = 144 \pm 6$ pc. These different estimates are all well within the confidence region of the original estimate, demonstrating that any systematic errors introduced by the choice of radial profile model are smaller than the quoted statistical error.

4.2. Comoving Radial Profile

The radial profile of the halo was examined in more detail by summing the five radial profiles (Fig. 3), after adjusting the size of the radial bins to correct for the expansion of the halo. A constant background level, estimated from the mean level at large radii, was subtracted from each profile before combining them. The result is shown in Figure 6. This shows that the average radial profile of the halo, after correcting for its expansion, was reasonably narrow. Fitting this profile using a Gaussian to model the halo gave a relative width of FWHM(θ)/$\theta \approx 0.16$–0.23 (90% confidence limit).

The observed radial width of the halo is a combination of four terms: (1) the time profile of the illuminating X-ray pulse, (2) the radial distribution of the dust along the line of sight, (3) the PSF of the XRT, and (4) the radial expansion of the halo over the length of an exposure. Term 1 is negligible, since the time duration of the initial pulse is short compared to the times (since burst) of the halo images. The XRT PSF (with FWHM of $9''6$) gives rise to a fractional width of 20% in the first image to 5% in the last, meaning term 3 must contribute significantly to the measured width. The comoving radial profile is dominated by counts from later

images (with longer exposures), during which the fractional increase in the halo radius, term 4, was ~15%. The measured width of the halo may therefore be explained entirely by terms 3 and 4, implying that the remaining term, the radial thickness of the dust, must be small. A very conservative limit on the physical thickness of the dust cloud along this line of sight is $\Delta D \approx D \times$ FWHM(θ)/$\theta < 22$ pc. Most likely, the dust is confined in a much narrower region.

4.3. Halo Spectrum

The spectrum of the halo was extracted from the first orbit of data using an annular extraction region with inner and outer radii of 20 and 45 pixels ($47''$–$106''$), respectively. A background spectrum was extracted from an annulus with radii of 60 and 100 pixels, and an appropriate ancillary response file was generated. Due to the small number of counts (≈ 100) the spectrum was fitted using the C-statistic, rather than binning to 20 counts per bin and fitting using the χ^2 statistic, which would result in very few bins. The spectral model used was an absorbed power law, with the neutral absorption column density fixed at the value obtained from the early XRT spectrum ($N_H = 5.9 \times 10^{21}$ cm^{-2}; § 3). The data are shown in Figure 7. The best-fitting photon index was $\Gamma = 2.7^{+0.5}_{-0.3}$, significantly steeper than the GRB X-ray spectrum ($\Gamma = 1.94 \pm 0.05$), as expected due to the strong energy dependence of the dust-scattering cross section. The model gave a good fit, with a rejection probability of only $p = 0.31$ estimated using 10^3 Monte Carlo simulations. The mean photon energy in the binned, background-subtracted halo spectrum was $\langle E \rangle = 1.54$ keV.

4.4. Halo Flux as a Function of Angle

The flux decay of the halo was also estimated using the radial profile of the combined image from orbits 1 and 2 (over which the halo is well detected). Counts were accumulated in annuli of width $\Delta\theta = 17''6$ (7.5 pixels) and background subtracted assuming a constant background level per pixel estimated from an annulus enclosing $280''$–$370''$. The sampling of the halo as a function of angle is incomplete, due to the incomplete time coverage of the observation; therefore, radii over which the halo was not observed were masked out of the radial profile. The masking was done by converting the times of the observations into radii, using the best-fitting expansion curve (Fig. 5) and removing all radial bins containing unobserved angles. The result is shown in Figure 8.

---

[9] This distance estimate is smaller than that given in Romano et al. (2005) because that earlier analysis assumed $t_X = T_0$, an assumption not made here.
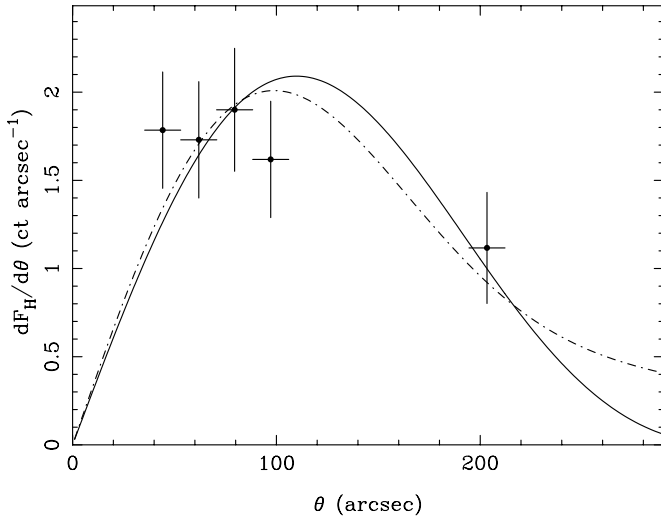
FIG. 8.—Halo flux as a function of scattering angle. The crosses show the background-subtracted counts per (equal size) radial bin over which the halo was detected. The solid curve marks the best-fitting theoretical scattering curve $dF_H/d\theta$ (eq. [3]), assuming a single grain size ($a = 0.367\ \mu$m). The dot-dashed line shows the best-fitting function assuming a MRN77 distribution of grain sizes (with $a_{\max} = 0.524\ \mu$m).

The total fluence of scattered light (in the halo), F_H, should be related to the direct light (i.e., unscattered light from the GRB), F_X, by:

$$\frac{F_H}{F_H + F_X} = 1 - e^{-\tau_{\mathrm{scat}}}, \qquad (1)$$

where $\tau_{\mathrm{scat}} = \sigma N_g$ is the scattering optical depth, with σ the total scattering cross section, and N_g is the dust grain column density along the LOS (e.g., eq. [14] of Mauche & Gorenstein 1986, hereafter MG86). For low optical depths ($\tau_{\mathrm{scat}} \ll 1$), at which multiple scattering is insignificant, this can be approximated by $F_H \approx \tau_{\mathrm{scat}} F_X$. The above quantities represent the entire halo (integrated over all scattering angles), but the scattering cross section is a function of angle, which defines the halo fluence per unit angle. In the Rayleigh-Gans approximation[10] the differential scattering cross section for a spherical grain of size a (in units of microns) is given by (eq. [2.2] of Hayakawa 1970)

$$\frac{d\sigma}{d\Omega} = A_E a^6 \left[\frac{j_1(x)}{x}\right]^2 (1 + \cos^2\theta), \qquad (2)$$

where A_E is a normalization that depends on the energy of X-rays being scattered, $x = (4\pi a/\lambda)\sin(\theta/2)$, and $j_1(x) = (\sin x)/x^2 - (\cos x)/x$ is the spherical Bessel function of the first order. The central core of this function is approximately Gaussian, leading to a halo with a characteristic size $\theta_{\mathrm{rms}} \approx 62.4(aE)^{-1}$ arcsec (eq. [6] of MG86; Hayakawa 1970). Using equation (2) the scattered fluence in the halo per unit scattering angle is

$$\frac{dF_H}{d\theta} = A_E a^6 2\pi\theta \left[\frac{j_1(x)}{x}\right]^2 (1 + \cos^2\theta) N_g F_X$$

$$\propto a^6 \theta \left[\frac{j_1(x)}{x}\right]^2 (1 + \cos^2\theta), \qquad (3)$$

which peaks at $\theta \approx \theta_{\mathrm{rms}}$.

This function was fitted to the data (Fig. 8, *solid curve*), yielding a best-fitting value of $a = 0.367\ \mu$m (with a 90% confidence region of 0.316–0.430 μm), assuming a typical energy of $E \approx 1.54$ keV for the scattered X-rays (see § 4.3). The scattering of soft X-rays is dominated by the largest grains, due to the strong dependence of the scattering cross section on grain size (the total scattering cross section, integrated over all angles, is $\sigma \propto a^4$), and so this estimate for a corresponds to grains close to the maximum grain size. This best-fitting model was integrated over all angles to estimate the total halo fluence of $F_H \approx 342 \pm 34$ counts (where the 1 σ error was approximated by the 10% fractional error on the total observed halo fluence).

The above calculation is valid for a single grain size, which should be a reasonable approximation given the strong dependence of the scattering cross section on a. The presence of smaller grains will, however, cause the halo fluence to fall off less rapidly at large angles, and this extended "tail" could contain substantial additional fluence. In order to investigate the consequence of a continuous grain size distribution, equation (3) was recalculated at each angle by integrating over the grain size distribution $N(a)$. The size distribution was assumed to follow that of Mathis et al. (1977; hereafter MRN77),

$$N(a) = \begin{cases} N_0 a^{-q}, & a_{\min} \le a \le a_{\max}, \\ 0, & \text{elsewhere.} \end{cases} \qquad (4)$$

The revised function was fitted to the data assuming $a_{\min} \approx 0.04\ \mu$m and $q = 3.5$, yielding a best-fitting $a_{\max} = 0.524\ \mu$m (with a 90% confidence region, 0.426–0.790 μm); this is slightly larger than, but not inconsistent with, other estimates derived from X-ray halos (MG86; Predehl et al. 1991; Clark 2004). The best-fitting model is also shown in Figure 8 (*dot-dashed curve*). The fit is not very sensitive to $a_{\min}$ as long as $a_{\max}/a_{\min} \gtrsim 5$ and $q \gtrsim 3.5$.[11] The total fluence in this model, integrated over all angles, was virtually identical to the single grain size model ($\approx 343 \pm 34$ counts), although the fluence could be higher if there is a greater contribution from smaller grains scattering to larger angles that were not directly observed.

4.5. Scattering Optical Depth

Given the above estimate of the halo fluence, F_H, it is possible to estimate the dust-scattering optical depth once the direct GRB X-ray fluence, F_X, is known. This latter quantity can be estimated by integrating the combined XRT/BAT light curve of the burst. Figure 3 of Barthelmy et al. (2005) shows the X-ray light curve of GRB 050724 from T_0. This was produced using the XRT observations after $T_0 + 79$ s and the 15–25 keV BAT light curve extrapolated into the XRT band based on a spectral fit to the simultaneous BAT and XRT spectrum. During the first $\sim$300 s after the trigger, the X-ray source was bright; the WT data contain $\sim 1.18 \times 10^4$ source counts (0.2–10 keV). The extrapolated BAT data predict almost exactly the same number of counts prior to the start of the XRT/WT observation. Although there will be a systematic error associated with the extrapolation of the BAT data to lower energies, the tight agreement between BAT and XRT data in the interval of overlap suggests that this is likely to be small (Barthelmy et al. 2005). Together, these give a total of $\approx 2.42 \times 10^4$ counts. Combining this with the F_H value of § 4.4 gives $\tau_{\mathrm{scat}} \approx F_H/F_X \approx 0.014$. Making an approximate correction to an

---

[10] Smith & Dwek (1998) demonstrated that the Rayleigh-Gans theory and the more exact Mie theory are in close agreement for photon energies $E \approx 2$ keV and typical grain sizes.

[11] Using $a_{\min} = 0.004$ or 0.1 μm changed the fit statistic by only $\Delta\chi^2 = +0.009$ or $+0.038$, respectively.
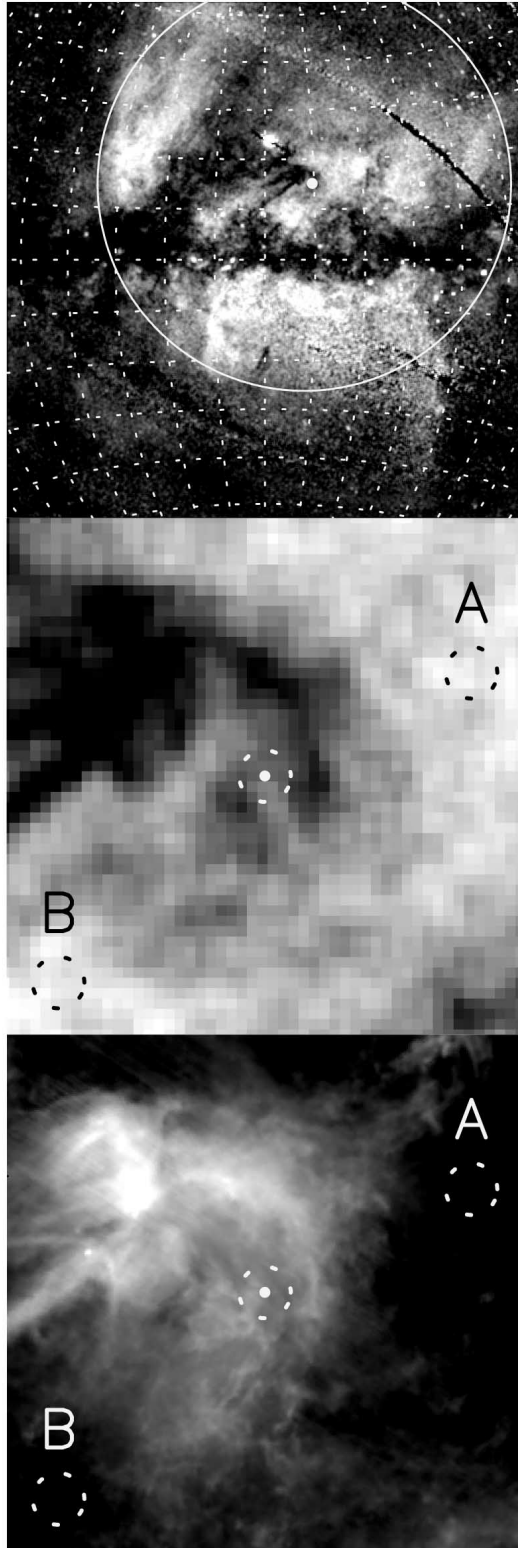
VAUGHAN ET AL.

FIG. 9.—X-ray and IR images of the sky around GRB 050724. *Top*: 0.4–1.2 keV RASS map in Galactic coordinates spanning 102° on a side. The position of GRB 050724 is marked with the small white filled circle; the large circle marks the extent of the superbubble centered on the Sco-Cen OB association. *Middle*: 10° × 10° close up of the RASS map around GRB 050724 (marked with the white filled circle). The dotted circle has a radius of 0°5, which corresponds to ≈2.4 pc at the distance to the scattering dust. *Bottom*: 100 μm *IRAS* map on the same scale as the middle panel. Clearly, the IR emission and soft X-ray absorption are well correlated. Again, the position of the GRB is indicated by the white filled circle. Positions A and B mark the off-cloud regions discussed in the text. [*See the electronic edition of the Journal for a color version of this figure.*]

effective scattering optical depth at 1 keV gives $\tau_{\mathrm{scat}}(1\ \mathrm{keV}) \approx \tau_{\mathrm{scat}}(E)E^2 = 0.034$ (with E being the mean scattered photon energy in kilo–electron volts).

5. ISM TOWARD GRB 050724

Archival *ROSAT* and *IRAS* data were used to constrain the ISM in the direction of GRB 050724. The top two panels of Figure 9 show the soft X-ray sky around GRB 050724, derived from the *ROSAT* all-sky survey (RASS) data in the 0.4–1.2 keV band, and the bottom panel shows the *IRAS* all-sky survey 100 μm map of the region. These images reveal structures dominated by the Ophiuchus molecular cloud complex casting the dark "shadows" in the *ROSAT* map (Fig. 9, *middle*) and enhanced IR dust emission in the *IRAS* map (Fig. 9, *bottom*). The main ρ Oph molecular cloud (L1688; Klose 1986) is the bright region in the upper left part of the *IRAS* map. These data were used to estimate the column density in the cloud by comparing the column density estimates for the GRB position to those at locations A and B, chosen to be representative of nearby but off-cloud lines of sight.

The column densities were estimated in three independent ways, and the results are presented in Table 1. The first estimate comes from the Dickey & Lockman (1990) 21 cm maps of N_{H}. This shows little change in N_{H} between the three positions (see Table 1), and this was confirmed by the 21 cm map of the region shown by de Geus & Burton (1991; see their Fig. 5). The column density due to the intervening cloud in the direction of GRB 050724 was estimated from the difference between the column density toward the GRB and the mean of that measured for A and B. This gave $N_{\mathrm{H}} = (0.05 \pm 0.20) \times 10^{21}$ cm^{-2} (where the uncertainty is a very rough estimate based on half the difference between A and B). In other words, there is no excess H i in the direction of GRB 050724 due to the intervening dust cloud.

The second estimate comes from the IR reddening maps from Schlegel et al. (1998). This gave $E(B-V)$ values, based on the *Cosmic Background Explorer* (*COBE*) temperature and *IRAS* intensity at the position of interest, of 0.59, 0.17, and 0.25 for the GRB, A, and B, respectively. These correspond to optical extinctions of $A_V = 2.37$, 0.68, and 1.01, respectively, assuming $R_V \equiv A_V/E(B-V) = 4.0$, as measured by Vrba et al. (1993) in the direction of the ρ Oph cloud. The reddening values were converted to hydrogen column densities assuming $N_{\mathrm{H}} = 4.93 \times 10^{21} E(B-V)$ cm^{-2} (Diplas & Savage 1994). In this case the excess column density over the GRB was $N_{\mathrm{H}} = (1.9 \pm 0.2) \times 10^{21}$ cm^{-2}. However, as noted by Jura (1980), Vuong et al. (2003), and others, the dust-to-gas conversion factors in the direction of the Oph cloud are uncertain due to the complexity of modeling the cloud medium.

The third estimate was derived from RASS spectra extracted using 0°5 radius regions centered on the positions of the GRB, A, and B.[12] These were fitted with the model developed by Willingale

[12] *ROSAT* count rates in different channels were extracted using the HEASARC X-ray background tool available at http://heasarc.gsfc.nasa.gov/.

TABLE 1
COMPILATION OF GALACTIC COLUMN DENSITY ESTIMATES

Technique	Reference	N_{H} [GRB] (10^{21} cm^{-2})	N_{H} [A] (10^{21} cm^{-2})	N_{H} [B] (10^{21} cm^{-2})
21 cm	1	1.46	1.22	1.61
IR map	2	2.92	0.83	1.24
RASS.............	3	3.57	0.52	1.28

REFERENCES.—(1) Dickey & Lockman 1990; (2) Schlegel et al. 1998; (3) This work.

et al. (2003) but, due to the complexity of the model and low resolution of the data, most parameters were fixed at the values found from an analysis of nearby *XMM-Newton* fields (M. A. Supper 2006, in preparation). The two parameters allowed to vary in the fit were the foreground-absorption column density and the emission measure of the "loop I superbubble" (indicated by the large circle in the top panel of Fig. 9). The excess column density toward GRB 050724 was estimated, by comparison with A and B, at $N_{\rm H} = (2.7 \pm 0.4) \times 10^{21}$ cm^{-2}. Given the systematic errors involved in modeling the complex X-ray spectrum, and converting from a dust-reddening factor to equivalent hydrogen column density, the X-ray and IR derived estimates are in reasonable agreement.

6. DISCUSSION

The X-ray halo around GRB 050724, as observed by the *Swift* XRT, has provided accurate information on the Galactic dust distribution in this direction. In particular, the narrow halo must be caused by a concentration of dust at a distance of $D = 139 \pm 9$ pc from Earth, in a cloud or sheet with a thickness $\Delta D < 22$ pc. The radial profile of the halo constrains the size of the largest grains to be $a_{\rm max} \sim 0.4-0.5$ μm, but the contribution from smaller grains is unconstrained because the halo was not detected at scattering angles larger than $\theta \approx 200''$. The estimated value of $a_{\rm max}$ is higher than the often-used value of 0.25 μm (MRN77; see also Predehl & Schmitt 1995), although this is not without precedent, as Jura (1980) previously noted that the nonstandard optical extinction curves in the direction of ρ Oph may signify the presence of unusually large grains.

The LOS to GRB 050724 includes the Upper Scorpius subgroup of the Sco-Cen OB association at a mean distance of 145 ± 2 pc (derived from *Hipparcos* data; de Zeeuw et al. 1999). There is considerable structure in the extinction maps around this region, including material belonging to the Ophiuchus molecular cloud complex (de Geus 1992). Knude & Høg (1998) detected a sharp rise in the reddening at $120-150$ pc in the direction of the ρ Oph star-forming region, which is consistent with the distance measured for the dust responsible for the X-ray halo. If the X-ray-scattering dust is associated with part of the Oph molecular cloud complex, this gives the most accurate measurements to date for the distance to the cloud and its physical thickness.

The excess optical extinction in the direction of GRB 050724, compared to the mean of the off-cloud positions A and B, was $A_V = 1.5$ mag (§ 5). In combination with the estimated halo-scattering optical depth (§ 4.5) this gives $\tau_{\rm scat}/A_V \approx 0.022$ at 1 keV. This is lower than the value of 0.056 estimated by Predehl & Schmitt (1995) using *ROSAT* observations of bright Galactic X-ray

sources, and a factor of a few lower than the value derived from the model of Draine (2003). However, the halo around GRB 050724 was only observed at small angles ($\theta \lesssim 200''$), and so the flux contribution from smaller grains is largely unconstrained, meaning that the true halo flux, and hence $\tau_{\rm scat}$, is probably larger.

As shown by Figure 9, the X-ray absorption and IR dust emission are well correlated, demonstrating that they are caused by the same medium. By contrast, the 21 cm map shows little correlation with these images (Fig. 5 of de Geus & Burton 1991), suggesting that the cloud medium has a comparatively low density of atomic H I. The most obvious explanation is that the hydrogen is molecular, although there is no obvious CO emission from this location in Figure 3 of de Geus et al. (1990). The Lyα map of the region (see Fig. 13 of de Geus et al. 1990) shows two nearby H II regions, known as S9 and RCW 129, around the stars σ Sco (B1 III) and τ Sco (B0 V), respectively. It is therefore also plausible that some fraction of the atomic hydrogen is ionized by these nearby young stars (with distances of $\sim$140 pc; Shull & van Steenberg 1985). The total Galactic hydrogen column density along the LOS to GRB 050724 is therefore the sum of that revealed by the 21 cm H I maps and that inferred from the molecular cloud (mostly H$_2$ and/or H II). The 21 cm measurement of the total H I column density gave 1.5×10^{21} cm^{-2}, whereas the column density in the dust cloud was measured at $(1.9 \pm 0.2) \times 10^{21}$ cm^{-2} from the excess IR emission and $(2.7 \pm 0.4) \times 10^{21}$ cm^{-2} from the excess soft X-ray absorption (§ 5). The total hydrogen column density is therefore in the range $(3.4-4.2) \times 10^{21}$ cm^{-2}, slightly lower than that measured from the GRB X-ray spectrum [$(4.4-6.2) \times 10^{21}$ cm^{-2}; § 3]. It is of course possible that this extra X-ray absorption along the LOS to GRB 050724 ($\Delta N_{\rm H} \sim 1.5 \times 10^{21}$ cm^{-2}) is caused by either a modest column of molecular or ionized gas on the far side of the Sco-Cen superbubble, or is due to cold gas in the GRB host galaxy, the formal constraint on which was $N_{\rm H} < 2.4 \times 10^{21}$ cm^{-2} (§ 3).

REFERENCES

Alcock, C., & Hatchett, S. 1978, ApJ, 222, 456
Arnaud, K. 1996, in ASP Conf. Ser. 101, Astronomical Data Analysis Software and Systems V, ed. G. H. Jacoby & J. Barnes (San Francisco: ASP), 17
Barthelmy, S. D. 2004, Proc. SPIE, 5165, 175
Barthelmy, S. D., et al. 2005, Nature, 438, 994
Berger, E., et al. 2005, Nature, 438, 988
Burrows, D. N., et al. 2004, Proc. SPIE, 5165, 201
———. 2005a, Space Sci. Rev., 120, 165
———. 2005b, GCN Circ. 3697, http://gcn.gsfc.nasa.gov/gcn/gcn3/3697.gcn3
Cash, W. 1979, ApJ, 228, 939
Catura, R. C. 1983, ApJ, 275, 645
Clark, G. W. 2004, ApJ, 610, 956
Covino, S., et al. 2005, GCN Circ. 3665, http://gcn.gsfc.nasa.gov/gcn/gcn3/3665.gcn3
de Geus, E. J. 1992, A&A, 262, 258
de Geus, E. J., Bronfman, L., & Thaddeus, P. 1990, A&A, 231, 137
de Geus, E. J., & Burton, W. B. 1991, A&A, 246, 559

de Zeeuw, P. T., Hoogerwerf, R., de Bruijne, J. H. J., Brown, A. G. A., & Blaauw, A. 1999, AJ, 117, 354
Dickey, J. M., & Lockman, F. J. 1990, ARA&A, 28, 215
Diplas, A., & Savage, B. D. 1994, ApJ, 427, 274
Draine, B. T. 2003, ApJ, 598, 1026
Draine, B. T., & Bond, N. A. 2004, ApJ, 617, 987
Gal-Yam, A., et al. 2005, GCN Circ. 3681, http://gcn.gsfc.nasa.gov/gcn/gcn3/3681.gcn3
Gehrels, N., et al. 2004, ApJ, 611, 1005
Hayakawa, S. 1970, Prog. Theor. Phys., 43, 1224
Hill, J. E., et al. 2004, Proc. SPIE, 5165, 217
Jura, M. 1980, ApJ, 235, 63
Klose, S. 1986, Ap&SS, 128, 135
———. 1994, A&A, 289, L1
Knude, J., & Høg, E. 1998, A&A, 338, 897
Krimm, H., et al. 2005, GCN Circ. 3667, http://gcn.gsfc.nasa.gov/gcn/gcn3/3667.gcn3

Mathis, J. S., Rumpl, W., & Nordsieck, K. H. 1977, ApJ, 217, 425 (MRN77)
Mauche, C. W., & Gorenstein, P. 1986, ApJ, 302, 371 (MG86)
Miralda-Escudé, J. 1999, ApJ, 512, 21
Moretti, A., et al. 2004, Proc. SPIE, 5165, 232
———. 2005, Proc. SPIE, 5898, 348
Overbeck, J. W. 1965, ApJ, 141, 864
Predehl, P., Bräuniger, Burket, W., & Schmitt, J. H. M. M. 1991, A&A, 246, L40
Predehl, P., Burwitz, V., Paerels, F., & Trümper, J. 2000, A&A, 357, L25
Predehl, P., & Schmitt, J. H. M. M. 1995, A&A, 293, 889
Prochaska, J. X., et al. 2005, GCN Circ. 3700, http://gcn.gsfc.nasa.gov/gcn/gcn3/3700.gcn3
Rolf, D. P. 1983, Nature, 302, 46
Romano, P., et al. 2005, GCN Circ. 3685, http://gcn.gsfc.nasa.gov/gcn/gcn3/3685.gcn3
Schlegel, D. J., Finkbeiner, D. P., & Davis, M. 1998, ApJ, 500, 525

Shull, J. M., & van Steenberg, M. E. 1985, ApJ, 294, 599
Smith, R. K., & Dwek, E. 1998, ApJ, 503, 831
Soderberg, A. M., Cameron, P. B., & Frail, D. A. 2005, GCN Circ. 3684, http://gcn.gsfc.nasa.gov/gcn/gcn3/3684.gcn3
Tiengo, A., & Mereghetti, S. 2006, A&A, in press (astro-ph/0511186)
Trümper, J., & Schönfelder, V. 1973, A&A, 25, 445
Tylenda, R. 2004, A&A, 414, 223
Vaughan, S., et al. 2004, ApJ, 603, L5
Vrba, F., Coyne, G., & Tapia, S. 1993, AJ, 105, 1010
Vuong, M. H., Montmerle, T., Grosso, N., Feigelson, E. D., Verstraete, L., & Ozawa, H. 2003, A&A, 408, 581
Willingale, R., Hands, A. D. P., Warwick, R. S., Snowden, S. L., & Burrows, D. N. 2003, MNRAS, 343, 995
Wilms, J., Allen, A., & McCray, R. 2000, ApJ, 542, 914

Note added in proof.—Since the completion of this paper Tiengo & Mereghetti (2006) have announced the detection of another dust-scattered X-ray halo around a GRB. This brings the total number of known GRB X-ray halos to three.